Photoacoustics 1 (2013) 68–73

Contents lists available at ScienceDirect

Photoacoustics

journal homepage: www.elsevier.com/locate/pacs

Research Article

Functional optoacoustic human angiography with handheld video rate three dimensional scanner

Xosé Luís Deán-Ben [a,b], Daniel Razansky [a,b,*]

[a] Institute for Biological and Medical Imaging (IBMI), Helmholtz Center Munich, Ingolstädter Landstraβe 1, 85764 Neuherberg, Germany
[b] Faculty of Medicine, Technical University of Munich, Ismaninger Straβe 22, 81675 Munich, Germany

ARTICLE INFO

Article history:
Received 16 July 2013
Received in revised form 20 September 2013
Accepted 30 October 2013

Keywords:
Optoacoustic imaging
Cardiovascular diagnostics
Functional and molecular imaging

ABSTRACT

Optoacoustic imaging provides a unique combination of high optical contrast and excellent spatial resolution, making it ideal for simultaneous imaging of tissue anatomy as well as functional and molecular contrast in deep optically opaque tissues. We report on development of a portable clinical system for three-dimensional optoacoustic visualization of deep human tissues at video rate. Studies in human volunteers have demonstrated powerful performance in delivering high resolution volumetric multispectral optoacoustic tomography (vMSOT) images of tissue morphology and function, such as blood oxygenation parameters, in real time. Whilst most imaging modalities currently in clinical use are not able to deliver volumetric data with comparable time resolution, the presented imaging approach holds promise to attain new diagnostic and treatment monitoring value for multiple indications, such as cardiovascular and peripheral vascular disease, disorders related to the lymphatic system, breast lesions, arthritis and inflammation.

1. Introduction

Ultrasonography is probably the most frequently used biomedical imaging tool in today's clinical practice [1], including cardiovascular diagnostics [2]. Among the major factors that have led to broad dissemination and clinical success of ultrasound imaging are non-ionizing excitation, real-time operation, handheld use and low cost. On the other hand, similarly to most traditional clinical imaging modalities, such as magnetic resonance imaging (MRI) and X-ray CT, ultrasound-based diagnostics mainly relies on anatomical appearance and other indirect functional indicators in order to deliver diagnostic value [3]. The need to track biological processes and disease state at the molecular level with high specificity and sensitivity has led to the development of positron emission tomography (PET) and single photon emission computerized tomography (SPECT) adding molecular imaging capabilities to medical diagnosis [4], while more recently extensive efforts are made to advance molecular imaging approaches in MRI [5,6] and ultrasound as well [7,8].

It is well accepted that the optical spectrum provides perhaps the best selection of approaches for tissue interrogation at the functional and molecular level [9]. With the recent emergence of methods appropriate for bio-marker in vivo staining, such as bioluminescence [10,11], fluorescent molecular probes [12,13] and proteins [14], as well as nanoparticle-based targeted agents [15–18], significant attention has been shifted toward interrogations of different dynamic biological processes in living specimens at the molecular level. Nevertheless, deep tissue optical imaging is severely affected by light scattering, limiting its in vivo use due to low imaging speed, poor spatial resolution and limited penetration [19]. The recent enormous progress on the development of hybrid optoacoustic imaging methods, including multispectral optoacoustic tomography (MSOT) approaches [20–23] are now poised to leverage the traditional contrast and specificity advantages of the optical spectrum. In optoacoustics, broadband ultrasound waves are generated due to absorption of ultrashort-duration pulses of light in tissue. Thus, it delivers a powerful set of both light- and ultrasound-related capabilities, including rich functional and molecular contrast, real-time operation and high spatial resolution, not affected by the scattering nature of biological tissues.

At present, the great potential of optoacoustic imaging that was showcased in preclinical research have encouraged translation of this technology into clinical practice with multiple applications envisioned, from cardiovascular [24] and cancer diagnostics [25] to

* Corresponding author at: Institute for Biological and Medical Imaging (IBMI), Helmholtz Center Munich, Ingolstädter Landstraβe 1, 85764 Neuherberg, Germany. Tel.: +49 8931871587; fax: +49 8931873063.
E-mail address: dr@tum.de (D. Razansky).

2213-5979
http://dx.doi.org/10.1016/j.pacs.2013.10.002

ophthalmology [26] and endoscopic imaging [27]. Nevertheless, while small animals are usually fully accessible for illumination and detection from multiple directions, due to the large dimensions, most parts of a human body can only be accessed from a single side. This imposes limitations on an optimal concurrent arrangement of the illumination and detection components, which are crucial for acquiring the desired quantification performance and image quality for a given application. For instance, adaptation of the common ultrasound linear array probes for optoacoustic imaging remains challenging, mainly due to fundamental differences in tomographic imaging requirements between ultrasound and optoacoustics, resulting in poor imaging performance and lack of sensitivity and quantification [28]. Furthermore, multiple additional technical limitations related to lack of appropriate ultrasound detection technology, digital sampling and processing capacities hindered so far the implementation of a hand-held 3D optoacoustic imaging system suitable for dynamic visualization of human pathology in the clinical setting.

Indeed, optoacoustics is ideal for delivering 3D real-time imaging capacity. This is because of its unique ability for generating complete volumetric tomographic datasets from the imaged object with a single interrogating laser pulse. This capacity comes with important clinical advantages. First, dynamic processes, such as the biodistribution of molecular probes, can be monitored in the entire volume of interest. Second, out-of-plane and motion artifacts that could degrade the image quality when imaging living specimen can be avoided. Finally, real-time 3D performance can obviously accelerate clinical observations.

2. Methods

2.1. Experimental setup

The developed clinical optoacoustic imaging system (Fig. 1) utilizes a hand-held probe design approach, which accommodates a custom-made two-dimensional array of 256 ultrasonic detectors (Imasonic SaS, Voray, France) arranged upon a spherical surface with a radius of 40 mm and covering a solid angle of 90 degrees [29]. In this way, the individual elements can most efficiently collect signals generated in the region of interest located around the center of the sphere. The individual transducer elements were manufactured using piezocomposite technology. They have a size of ca. 3 mm × 3 mm and 100% of available bandwidth around a central frequency of 4 MHz. In fact, the selected element size and the overall number of elements represents a hard compromise between real-time imaging performance (which requires larger element size to achieve higher SNR), design complexity (smaller number of elements) and image quality requirements (smaller element size and greater number of elements). Indeed, due to their relatively large size as compared to the detected ultrasound wavelengths, the elements present a frequency-dependent directivity pattern, which in turn limits their acceptance angle. Yet, orientation of the elements toward the center of the sphere optimizes the angular tomographic coverage and overall sensitivity in this region [30]. Since many clinical imaging scenarios, such as imaging of large areas of human body, do not allow full tomographic access to the imaged area from all directions, this arrangement is particularly advantageous for optoacoustic imaging as the generated signals are optimally collected from as broad as possible range of angles (projections) around the imaged area located inside the living subject. The excitation light from a pulsed laser is delivered to the object through silica fused-end fiber bundle (CeramOptics GmbH, Bonn, Germany) inserted into a hole located in the center of the detection array. The bundle guides the light beam generated with a wavelength-tunable (690–900 nm) optical parametric oscillator (OPO) laser (Phocus, Opotek Inc., Carlsbad, CA) emitting short laser pulses (<10 ns duration) with a pulse repetition rate of 10 Hz. A transparent polyethylene membrane is used to enclose the active detection surface while the volume between the membrane and the active surface is further filled with matching fluid (water) in order to facilitate optimal acoustic coupling to the imaged object. Raw optoacoustic data are simultaneously sampled from all the detectors at 40 megasamples per second using a custom-made data acquisition system (Falkenstein Mikrosysteme GmbH, Taufkirchen, Germany), consisting of 256 parallel analog to digital converters arranged in 16 acquisition cards with 16 channels each, which is triggered by the Q-switch of the laser.

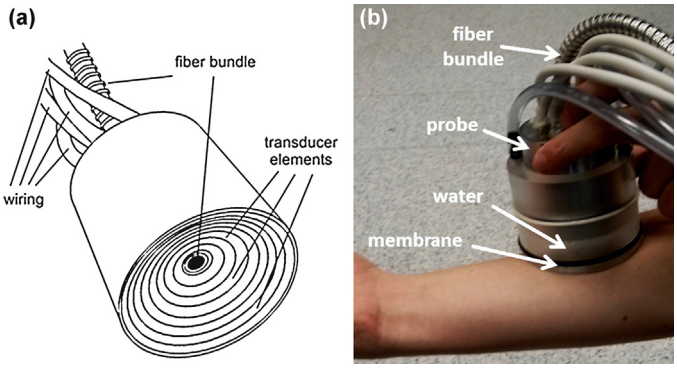

Fig. 1. Layout and color photograph of the clinical hand-held vMSOT probe for high resolution 3D (volumetric) imaging at video rate.

2.2. Image reconstruction

Prior to image reconstruction, the signals are band-pass filtered with cut-off frequencies 0.2–7 MHz and deconvolved with the electrical impulse response of the transducer. The volumetric optoacoustic images, representing spatial distribution of the absorbed optical energy, are obtained with a graphics processing unit (GPU) implementation of the three dimensional back-projection algorithm [29]. For accurate image reconstruction and spectral processing of multi-spectral data, a three dimensional model-based reconstruction algorithm [31] is applied instead for reconstructing the images at each wavelength. In short, the algorithm consists in a trilinear-interpolation-based discretization of the optoacoustic forward model in the time domain followed by numerical inversion by means of the Paige-Saunders iterative least-square algorithm based on QR factoriation (LSQR) [32] and standard Tikhonov regularization. The computations were executed on a workstation computer 2x Intel Xeon DP X5650 (6 × 2.67 GHz) with 144 GB of RAM.

2.3. Estimation of functional parameters

Spectral fitting of the images retrieved at several wavelengths is used to provide concentration maps of intrinsic tissue chromophores, such as oxygenated and deoxygenated hemoglobin, as well as other bio-markers. In order to estimate functional tissue parameters, i.e. blood oxygenation levels, it is assumed that the dominant tissue absorption in the considered wavelength range originates from two main intrinsic chromophores, melanin and hemoglobin in its oxygenated (HbO_2) and deoxygenated (HbR) forms. Thereby, by neglecting spectral variations of the light fluence distribution, the spatial distribution of the absorbed optical energy $H(\mathbf{x}, \lambda_m)$ in arbitrary units (assuming a constant Grüneisen parameter) for the N excitation wavelengths ($m = 1,\ldots,N$) is given

by a linear combination of the three chromophoric components [20], i.e.

$$H(\mathbf{x},\lambda_m) = \Phi(\mathbf{x})[\varepsilon_{Mel}(\lambda_m)C_{Mel}(\mathbf{x}) + \varepsilon_{HbR}(\lambda_m)C_{HbR}(\mathbf{x}) + \varepsilon_{HbO2}(\lambda_m)C_{HbO2}(\mathbf{x})] \quad (1)$$

where $\varepsilon(\lambda_m)$ and $C(\mathbf{x})$ stand for molar extinction spectra and concentration of the corresponding tissue chromophore. $\Phi(\mathbf{x})$ represents the light fluence distribution for the wavelength range employed. The molar extinction spectra of melanin, oxygenated and deoxygenated hemoglobin are displayed in arbitrary units in Fig. 3c. As a first-order approximation, we assume the light fluence to be constant for all wavelengths employed and exponentially attenuated as a function of depth along the depth direction with absorption coefficient representing average soft tissue optical properties in the near-infrared [33]. After canceling out the light fluence distribution, Eq. (1) can be rewritten in a matrix form as

$$\mathbf{H}(\mathbf{x}) = \boldsymbol{\varepsilon}\mathbf{C}(\mathbf{x}) \quad (2)$$

where $\mathbf{H}(\mathbf{x})$ and $\mathbf{C}(\mathbf{x})$ are two vectors corresponding to the acquired optoacoustic images at different wavelengths (after correction for light attenuation) and concentration distributions of the three chromophoric substances, respectively, while $\boldsymbol{\varepsilon}$ is the spectral unmixing matrix. Concentrations of the chromophores are subsequently estimated on a per-pixel basis by least-square fitting the measured optical absorption $\mathbf{H_m}(\mathbf{x})$ to a linear combination of contributions from the three main tissue chromophores. This is done by means of pseudoinverse of $\boldsymbol{\varepsilon}$, i.e.,

$$\mathbf{C}(\mathbf{x}) = \boldsymbol{\varepsilon}^{+}\mathbf{H_m}(\mathbf{x}). \quad (3)$$

Image of blood oxygenation levels is subsequently calculated via

$$SO_2(\mathbf{x}) = \frac{C_{HbO_2}(\mathbf{x})}{C_{HbO_2}(\mathbf{x}) + C_{HbR}(\mathbf{x})}. \quad (4)$$

It is important to emphasize that, in order to improve accuracy of the above spectral unmixing procedure at different depths, the light attenuation was herein corrected to the first order using a simple exponential decay function. Nevertheless, tissue heterogeneity, wavelength-dependence of light attenuation and the presence of additional tissue chromophores and extrinsic agents may all introduce further errors in the estimation of oxygenation levels. Accounting for those is a topic of our intensive ongoing investigations.

3. Results

3.1. Spatial resolution of the hand-held scanner

Characterization of the spatial resolution performance of the hand-held scanner was done using an agar phantom containing a 50 μm diameter black absorbing microsphere (Cospheric LLC Santa Barbara, CA). The microsphere was positioned around the geometrical center of the spherical detection array and the phantom was moved in order to characterize the resolution of the system in different directions. For each position, the corresponding point-spread-function was calculated with the backprojection algorithm within a volume of 15 mm × 15 mm × 15 mm consisting of 300 × 300 × 300 reconstructed image voxels. The corresponding results revealed relatively isotropic resolution of the system. While the axial resolution was found to be in the range of 300–500 μm, the lateral resolution varied between 200–400 mm for a region of 5 mm around the central position of the spherical array [30].

3.2. Video-rate tracking of deep tissue vasculature in vivo

Three in vivo experiments were conducted in the forearm and fingers of a healthy volunteer. The pulsed laser fluence was kept below the exposure safety limits of 20 mJ/cm^2 in all experiments [34].

In the first experiment, sequences of single-wavelength images of the vasculature in the forearm were taken, which showcases the capacity of the system to track vasculature in real-time. The laser wavelength was set at the isosbestic point of hemoglobin (797 nm), for which the extinction coefficient of oxygenated and deoxygenated hemoglobin is approximately the same. In order to reduce surface artifacts, the hair was removed from around the region of interest prior to the experiment. Real-time sequences of three-dimensional images were acquired with a repetition rate of 10 volumetric frames per second (pulse repetition rate of the laser) by moving the hand-held probe along the region of interest for a total duration of about 1 min. Typical volumetric maximal intensity projection (MIP) images from the forearm region, taken at distinctive time points (snapshots), are shown in Fig. 2a. All data were acquired in real time without averaging. The actual imaging performance can be best appreciated in the full video (Supplementary Video 1), where real-time tracking of deep tissue morphology is demonstrated. In the video, only MIP frames are used without color coding for depth. The effective field of view of each individual volumetric frame is about 12 mm in each direction. By combining images taken at different time points, one can capture a larger region, as shown for example in Fig. 2b, with the corresponding photograph displayed in Fig. 2c. Here, the three dimensional image is further color-coded for depth to get a better impression of the volumetric vasculature distribution. While some subsurface vessels are readily seen in the images and correlate well with the visible vasculature in the arm, many deeper (invisible) vessels can be clearly identified as well. Furthermore, other highly absorbing structures, such as skin pigmentations, can be visualized.

It should be noted that the spatial resolution of the system is determined by the available bandwidth of the ultrasonic detector (4 MHz), corresponding to effective spatial resolution on the order of 200 μm. Therefore, this particular implementation is not intended for visualizing networks of small capillaries, which requires significantly higher resolution scale but on the other hand limits the effective imaging depth to several millimeters, reducing usability for most clinical applications. It is instead intended for deep tissue human imaging with effective penetration depth and field of view of up to several centimeters, depending on the particular acquisition parameters and optical properties of the imaged region.

3.3. Three-dimensional MSOT of blood oxygenation

In the second experiment, multi-wavelength imaging of the wrist was performed in order to build oxygenation profiles in deep tissues. For this, the excitation laser wavelength was varied in the near-infrared region between 700 and 860 nm with a 20 nm step. For quantitative estimation of oxygenation levels, image reconstruction was done with a three-dimensional model-based algorithm [29]. Five representative MIP images acquired at different wavelengths are shown in Fig. 3a. A movie file is available in the on-line version of the journal (Supplementary Video 2) showing the corresponding images for all the wavelengths used in the experiment. Overall, it can be seen that the pixel intensity increases with wavelength for some of the vessels (presumably arteries) while it remains more or less constant for the other vessels (presumably veins). This is indeed expected since the spectrum of fully oxygenated blood in the arteries shows a monotonous increase in this spectral region, whereas the

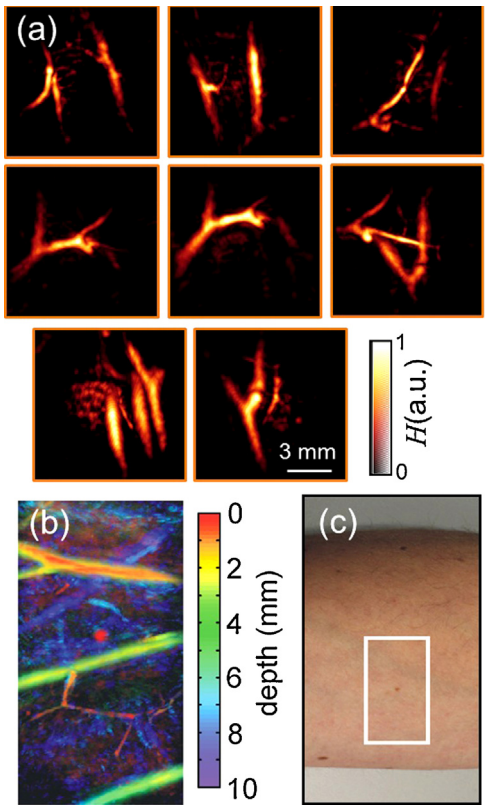

Fig. 2. Video-rate optoacoustic tracking of deep tissue vasculature in vivo, acquired by translating the probe over forearm of a healthy volunteer. (a) Single frame volumetric (maximum intensity projection along the depth direction) images acquired at distinctive time points. (b) A combined volumetric image of a larger region color-coded for depth and the corresponding imaged region (c).

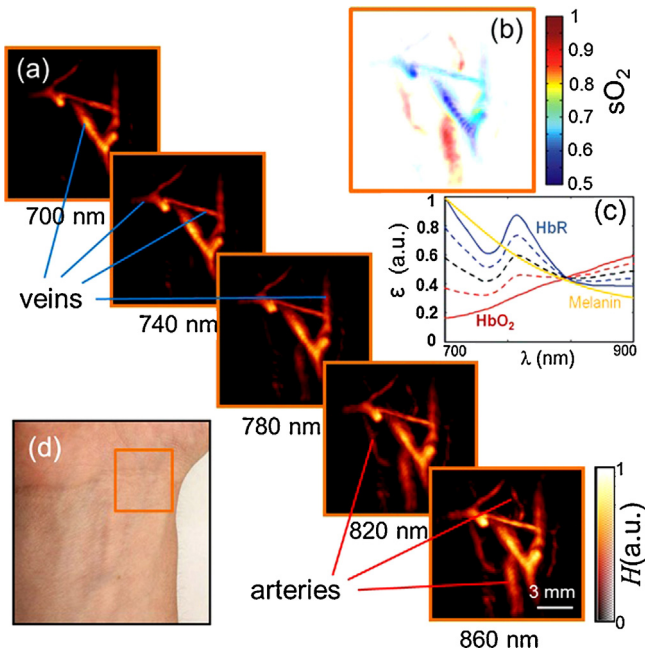

Fig. 3. Multispectral tomographic reconstructions of the wrist region. (a) Volumetric (maximum intensity projection along the depth direction) images acquired at 5 different wavelengths in the near-infrared. Two main types of vessels (arteries and veins) can be readily identified by their spectral behavior. (b) Map of blood oxygen saturation, as calculated from images acquired at the different wavelengths. (c) Extinction (absorption) spectra of major tissue chromophores in arbitrary units. The curves for hemoglobin are shown for 100% oxygenation (continuous red line), 75% oxygenation (dashed red line), 50% oxygenation (dashed black line), 25% oxygenation (dashed blue line) and 0% oxygenation (continuous blue line). (d) Color photograph of the imaged region.

spectra remain nearly constant for levels of around 50–75% oxygenation normally present in the veins. It can be noticed that the image at 700 nm has stronger background signal, presumably due to strongest absorption by the skin melanin at this wavelength as compared to the other (higher) wavelengths used in the experiment.

To confirm the visual findings, we performed spectral unmixing of the images acquired at all the 9 wavelengths. For unmixing using the previously described spectral fitting method, the known absorption spectra of oxygenated and deoxygenated hemoglobin (Fig. 3c) were used. The acquisition time in multispectral imaging is mainly conditioned by the time required to acquire data for all the wavelengths, which was about several seconds in the current experiment. Due to the hand-held probe design, the multi-spectral data might have still been affected by motion artifacts. Yet, the corresponding map of blood oxygenation accurately reveals location of the veins versus arteries (Fig. 3b).

3.4. Real-time imaging of hemodynamic changes

The last experiment illustrates capability of imaging dynamic processes in vivo. Herein, the circulation in the middle finger was obstructed by means of a rubber band approximately 30 s before the start of image acquisition. A sequence of single wavelength images was acquired during 100 s with the rubber band removed after approximately 42 s. The wavelength in this case was set to 900 nm, so that amplitude of the optoacoustic signals is increased both with blood volume and blood oxygenation.

The imaged region along with the volumetric images corresponding to seven time instants are shown in Fig. 4. A movie file is available in the on-line version of the journal showing the entire sequence of 100 images (Supplementary Video 3). Each movie frame was averaged over 10 consecutive laser pulses in the postprocessing for better visualization and noise reduction.

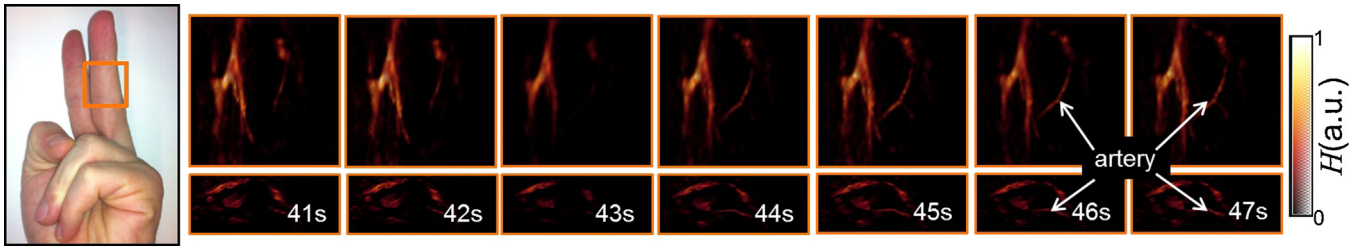

Fig. 4. Tomographic reconstructions of the vasculature in human finger in the region as indicated in the photograph on the left. The snapshots are shown for seven consecutive seconds around the time point when the rubber band, blocking the blood flow, was removed from the finger (ca. 42 s after the start of image acquisition).

4. Discussion

In this work we introduced the clinical imaging capabilities of a hand-held volumetric multispectral optoacoustic tomography (vMSOT) system capable of real-time optoacoustic imaging of intrinsic anatomical and functional contrast as well as extrinsically-administered bio-markers in deep tissues. The proposed hand-held design combined with the real-time (video-rate) performance further make it highly effective for in vivo biological and clinical imaging in areas such as cardiovascular and breast diagnostics, imaging of cancer, inflammation, and lymphatic system. The system utilizes a two-dimensional array of ultrasonic detectors arranged on a spherical surface, which is particularly useful for collecting optoacoustic responses from deeper areas of human body having no full tomographic access from all directions.

Real-time visualization of deep tissue morphology and function was demonstrated herein up to a depth of about 1 cm. It is hypothesized that, by optimizing light delivery and signal detection parameters and by using signal averaging, the imaging depth can be extended down to several centimeters in most soft tissues. In fact, other optoacoustic imaging studies, which however were not performed in real-time, have already demonstrated optoacoustic imaging of the entire human breast with typically imaged regions extending up to 5 cm [35]. While some other clinical imaging tools, such as ultrasound, MRI or CT, can penetrate deeper into tissues and ultimately provide whole-body human imaging capacity, the clear advantage of vMSOT is in its endogenous contrast, which does not only deliver high-resolution tissue morphology, but also provides highly valuable functional and, potentially, targeted molecular information important for clinical decision making. Indeed, the light-based contrast advantage of optoacoustics is further greatly supported by the significantly broader selection of contrast agent approaches available for the light-based methods versus other imaging modalities. As has been also demonstrated, vMSOT is essentially a three-dimensional real time imaging method, a feature difficult to achieve with other imaging approaches.

Several aspects of system performance require further attention. While a laser pulse repetition frequency of 10 Hz is been currently used, higher repetition rates will further improve the time resolution of the system. This, in turn, will further facilitate rejection of motion artifacts and overall improvement in the image quantification capacity. However, due to laser safety limitations, faster repetition rates may force using lower per-pulse energy levels so that both per pulse laser fluence and average power density limitations are met [34]. Lower per-pulse energies may consequently lead to reduction of image quality and effective penetration depth for real time imaging due to lower SNR of the acquired data. Nevertheless, visualization of spectrally dependent tissue chromophores and extrinsic contrast agents necessitates collection of multiwavelength data, which currently requires up to a few seconds. Having lasers with fast wavelength tuning capability would therefore greatly facilitate visualization of functional parameters in real time.

Overall, it is expected that the powerful performance of the developed handheld vMSOT approach will define several new application areas, further making it an indispensable imaging tool in selected clinical segments.

Acknowledgements

The research leading to these results received funding from the European Research Council under grant agreement *ERC-2010-StG-260991*.

Conflict of interest statement

The authors declare that there are no conflicts of interest.

Appendix A. Supplementary data

Supplementary data associated with this article can be found, in the online version, at doi:10.1016/j.pacs.2013.10.002.

References

[1] McGahan JP, Goldberg BB. Diagnostic ultrasound. Informa UK Ltd.; 2008.
[2] Devuyst G, et al. Ultrasound measurement of the fibrous cap in symptomatic and asymptomatic atheromatous carotid plaques. Circulation 2005;111:2776–82.
[3] Kelley LL, Petersen CM. Sectional anatomy for imaging professionals. St. Louis, MO: Mosby; 2012.
[4] Von Schulthess GK. Molecular anatomic imaging: pet-CT and spect-CT integrated modality imaging. Philadelphia, PA: Lippincott Williams & Wilkin; 2007.
[5] Lee JH, et al. Artificially engineered magnetic nanoparticles for ultra-sensitive molecular imaging. Nature Medicine 2007;13:95–9.
[6] Ghosh D, et al. M13-templated magnetic nanoparticles for targeted in vivo imaging of prostate cancer. Nature Nanotechnology 2012;7:677–82.
[7] Ryu JC, et al. Molecular imaging of the paracrine proangiogenic effects of progenitor cell therapy in limb ischemia. Circulation 2012;127:710.
[8] Lindner JR. Molecular imaging of cardiovascular disease with contrast-enhanced ultrasonography. Nature Reviews Cardiology 2009;6:475–81.
[9] Weissleder R, Pittet MJ. Imaging in the era of molecular oncology. Nature 2008;452:580–9.
[10] Luker KE, et al. In vivo imaging of ligand receptor binding with Gaussia luciferase complementation. Nature Medicine 2012;18:172–7.
[11] Suter DM, et al. Mammalian genes are transcribed with widely different bursting kinetics. Science 2011;332:472–4.
[12] Kobayashi H, Ogawa M, Alford R, Choyke PL, Urano Y. New strategies for fluorescent probe design in medical diagnostic imaging. Chemical Reviews 2010;110:2620–40.
[13] Schaferling M. The art of fluorescence imaging with chemical sensors. Angewandte Chemie International Edition 2012;51:3532–54.
[14] Shu XK, et al. Mammalian expression of infrared fluorescent proteins engineered from a bacterial phytochrome. Science 2009;324:804–7.
[15] Ghosh S, Bachilo SM, Simonette RA, Beckingham KM, Weisman RB. Oxygen doping modifies near-infrared band gaps in fluorescent single-walled carbon nanotubes. Science 2010;330:1656–9.
[16] Cobley CM, Chen JY, Cho EC, Wang LV, Xia YN. Gold nanostructures: a class of multifunctional materials for biomedical applications. Chemical Society Reviews 2011;40:44–56.
[17] Shang L, Dong SJ, Nienhaus GU. Ultra-small fluorescent metal nanoclusters: synthesis and biological applications. Nano Today 2011;6:401–18.
[18] Kircher MF, et al. A brain tumor molecular imaging strategy using a new triple-modality MRI-photoacoustic-Raman nanoparticle. Nature Medicine 2012;18. 829-U235.
[19] Wang LV, Wu H-I. Biomedical optics: principles and imaging. Hoboken, NJ: Wiley; 2007.
[20] Razansky D, et al. Multispectral opto-acoustic tomography of deep-seated fluorescent proteins in vivo. Nature Photonics 2009;3:412–7.
[21] Ntziachristos V, Razansky D. Molecular imaging by means of multispectral optoacoustic tomography (MSOT). Chemical Reviews 2010;110:2783–94.
[22] Razansky D, Buehler A, Ntziachristos V. Volumetric real-time multispectral optoacoustic tomography of biomarkers. Nature Protocols 2011;6:1121–9.
[23] Wang LHV, Hu S. Photoacoustic tomography: in vivo imaging from organelles to organs. Science 2012;335:1458–62.
[24] Razansky D, et al. Multispectral optoacoustic tomography of matrix metalloproteinase activity in vulnerable human carotid plaques. Molecular Imaging and Biology 2012;14:277–85.
[25] Buehler A, et al. High resolution tumor targeting in living mice by means of multispectral optoacoustic tomography. EJNMMI Research 2012;2:14.
[26] Jiao S, et al. Photoacoustic ophthalmoscopy for in vivo retinal imaging. Optics Express 2010;18:3967–72.
[27] Yang JM, et al. Simultaneous functional photoacoustic and ultrasonic endoscopy of internal organs in vivo. Nature Medicine 2012;18:1297–302.
[28] Buehler A, et al. Model-based optoacoustic inversions with incomplete projection data. Medical Physics 2011;38:1694–704.
[29] Dean-Ben XL, Ozbek A, Razansky D. Volumetric real-time tracking of peripheral human vasculature with GPU-accelerated three dimensional optoacoustic tomography. IEEE Transactions on Medical Imaging 2013;32:2050–5.
[30] Dean-Ben XL, Razansky D. Portable spherical array probe for volumetric real-time optoacoustic imaging at centimeter-scale depths. Optics Express 2013;21:28062–71.
[31] Dean-Ben XL, Buehler A, Ntziachristos V, Razansky D. Accurate model-based reconstruction algorithm for three-dimensional optoacoustic tomography. IEEE Transactions on Medical Imaging 2012;31:1922–8.
[32] Paige CC, Saunders MA. LSQR. An algorithm for sparse linear equations and sparse least squares. ACM Transactions on Mathematical Software 1982;8:43–71.
[33] Jacques SL. Optical properties of biological tissues: a review. Physics in Medicine & Biology 2013;58:R37–61.
[34] American National Standards for the Safe Use of Lasers ANSI Z136.1. American Laser Institute; 2000.

[35] Heijblom M, et al. Visualizing breast cancer using the Twente photoacoustic mammoscope: what do we learn from twelve new patient measurements? Optics Express 2012;20:11582–97.

Xosé Luís Deán Ben received the diploma in automatics and electronics engineering from the *Universidade de Vigo* in 2004. He received the PhD degree from the same university in 2009. Since 2010, he serves as a postdoctoral fellow at the Lab for Optoacoustics and Molecular Imaging Engineering at the Institute for Biological and Medical Imaging (IBMI), Helmholtz Center Munich. His major research interests are the development of new optoacoustic systems for preclinical and clinical applications and the elaboration of mathematical algorithms for fast and accurate imaging performance.

Daniel Razansky is the Professor of Molecular Imaging Engineering at the Technical University of Munich and Director of the Lab for Optoacoustics and Molecular Imaging at the Institute for Biological and Medical Imaging, Helmholtz Center Munich. He earned his degrees in Electrical and Biomedical Engineering from the Technion—Israel Institute of Technology and completed a postdoctoral training at the Harvard Medical School. The research at his Lab lies at the forefront of the rapidly evolving area of molecular imaging sciences. The particular focus is on the development of novel biomedical imaging tools based on optoacoustics, diffuse optics, ultrasound, and multi-modality approaches in order to enable imaging with high spatial and temporal resolution on different scales, from organ to cell.